Available online at www.sciencedirect.com
ScienceDirect
Trans. Nonferrous Met. Soc. China 32(2022) 3901−3913
Transactions of Nonferrous Metals Society of China
www.tnmsc.cn

Effect of rolling reduction on deformation mechanism and twinning behavior of WE43 magnesium alloy

Qian-kun LI[1,2], Hong YAN[1,2], Rong-shi CHEN[1,2]

1. Shi-changxu Innovation Center for Advanced Materials, Institute of Metal Research, Chinese Academy of Sciences, Shenyang 110016, China;
2. School of Materials Science and Engineering, University of Science and Technology of China, Shenyang 110016, China

Received 19 October 2021; accepted 27 December 2021

Abstract: The effect of rolling reduction of the last pass on the dislocation slip and twinning behavior during direct hot rolling of a cast WE43 magnesium alloy at 480 °C was investigated. The results showed that prismatic $\langle a \rangle$ slip was always the main deformation mode during rolling at 480 °C. In addition, the activated twinning type was associated with rolling reduction. The $\{10\bar{1}2\}$ extension twinning was activated at a slight rolling reduction (2%), while $\{10\bar{1}1\}$ compression twinning and $\{10\bar{1}1\}-\{10\bar{1}2\}$ double twinning were activated at larger rolling reduction (12% and 20%). Schmid factor calculation showed that the activation of $\{10\bar{1}2\}$ extension twin variants followed the Schmid Law, whereas the activation of $\{10\bar{1}1\}$ compression twin variants did not follow it. Even if the rolling reduction reached 20%, almost no dynamic recrystallization (DRX) grains were found, presumably because the amount of deformation required for DRX to occur was not reached.

Key words: magnesium alloy; deformation; twin variants; recrystallization

1 Introduction

Due to their low density, high specific strength, and excellent vibration damping properties, magnesium alloys have become the most promising lightweight structural material and are widely used in automotive, aerospace, and other areas to reduce weight and save fuel [1−3]. However, the strength of commercial magnesium alloys such as AZ80 and ZK61 is lower than that of traditional metal materials such as aluminum alloys, steel and titanium alloys [4,5]. In recent years, rare earth (RE)-containing magnesium alloys have received significant attention because of their higher strength and good heat resistance due to the addition of RE elements [6−8]. WE43 magnesium alloy is one of the most promising RE-containing magnesium alloys due to its excellent mechanical and heat resistant properties [9]. Grains refinement is the best way to increase the strength and toughness of magnesium alloys [10−12], as the Hall−Petch coefficient of magnesium is four times that of aluminum [10]. And thermo-mechanical deformation, such as extrusion and rolling, is applied to WE43 magnesium alloys to refine grains and enhance strength [6]. However, the addition of RE elements improves the strength and heat resistance at the cost of significantly reducing the hot workability of RE-containing magnesium alloy [13,14]. Thereafter, extrusion is usually performed before rolling to refine grains and enhance the rollability of WE43

Corresponding author: Hong YAN, Tel: +86-24-23915897, Fax: +86-24-23894149, E-mail: hyan@imr.ac.cn;
Rong-shi CHEN, Tel: +86-24-23926646, Fax: +86-24-23894149, E-mail: rschen@imr.ac.cn
DOI: 10.1016/S1003-6326(22)66066-7

alloys, resulting in dimensional limitations of the sheet [6,15]. Besides, deformation behavior and mechanisms during the direct rolling of the cast alloys and extruded alloys are different due to different initial grain sizes. The larger grain size is prone to twinning and recrystallization. Differently, when the grain size is small, grain rotation mediates deformation, twinning is harder to be activated and pile-up of dislocation is reduced due to the lack of sufficient slip travel. Based on the difference in deformation behavior between extruded and cast alloys, it is necessary to investigate the deformation mechanism during the direct rolling of cast WE43 alloy.

Thermo-mechanical processing of RE-free magnesium alloys produces strong basal texture and increases anisotropy, e.g., rolling of AZ series magnesium alloys [16,17], which limits their deformability. The addition of RE elements to magnesium alloys can effectively weaken texture and refine grains due to the solute drag and the particle stimulated nucleation (PSN) mechanism during thermo-mechanical processing [18,19]. MACKENZIE et al [20] found that the second phase particles in the WE43 alloy were not deformed and caused strain concentrations around these hard particles. These zones were known as deformation zones and served as recrystallization sites, resulting in a weakened texture. Hence, the weak basal texture in as-rolled WE43 sheets was attributed to the PSN mechanism due to the addition of RE elements [21].

Most research work on WE43 rolling has been focusing on the extruded alloy with fine micro-structure. However, the deformation mechanism and twinning behavior during direct rolling of cast WE43 alloy with large grains have rarely been mentioned, which are important to the workability and mechanical properties of the rolled sheets with large scales [22−24]. The results of our previous work show that the rolled plates usually have no cracking at a total rolling reduction below 70%, after that rolling reduction was especially important for the integrity of the rolled plates. Therefore, the main purpose of this work is to understand the effect of rolling reduction at the last pass on the deformation mechanism, twinning behavior and texture evolution of WE43 alloy during direct rolling from the cast state at 480 °C.

2 Experimental

2.1 Material preparation

The WE43 magnesium alloy following the ASTM B80-15 was prepared, and the chemical composition was Mg−3.77Y−2.38Nd−1.45Gd−0.47Zr (wt.%) by inductively coupled plasma atomic emission spectroscopy (ICP-AES). Pure magnesium (99.95%), yttrium (99.95%), neodymium (99.95%), gadolinium (99.95%) and Mg−30Zr (wt.%) master alloys were melted in a resistance furnace using vacuum melting and argon protection, and the alloy was cast using low-pressure casting. Three square plates with the sizes of 200 mm × 100 mm × 15 mm were cut from the casting plate, and they were solution treated at 525 °C for 8 h. Then, they were rolled at 480 °C with a rolling reduction of 20% per pass at first six passes, and finally were rolled with different rolling reductions of 2%, 12% and 20%, respectively, which were named as specimen 1 (S1), specimen 2 (S2) and specimen 3 (S3). There was no change in rolling direction (RD) during the intermediate rolling process. The plates were reheated at 480 °C for 30 min after each pass and cooled in the air to room temperature after the last pass.

2.2 Microstructure characterization

The microstructures were observed by optical microscope (OM) and scanning electron microscope (SEM, Philips XL30 ESEM-FEG/EDAX). OM specimens cut from the as-rolled WE43 alloy were etched in a solution of nitric acid and alcohol after mechanical polishing. The macro-texture was measured by X-ray diffraction (Rigaku D/max2400) at an angle of 0°−70° on a specimen with a size of 20 mm × 22 mm, and the data were analyzed using DIFFRACplus TEXEVAl software. EBSD observation was carried out using a Hitachi Se3400 N SEM equipped with an HKL-EBSD system at an applied voltage of 20 kV and a probe current of 60 nA. The scan steps used for the three specimens were different because of the different grain sizes, with S1 having a step size of 3 μm, and S2 and S3 having a step size of 1.2 μm. Moreover, the hit rate of all specimens was above 90%. The hardness test was carried out using a Vickers hardness tester with a loading force of 500 g and a loading time of 10 s.

3 Results

3.1 Microstructure of WE43 alloy in solution state

The microstructure of solution-treated (525 °C for 8 h) WE43 alloy is presented in Fig. 1. After solution-treatment, the average grain size of the alloy increased up to ~92 μm compared with the as-cast alloy (~42 μm) measured by the linear intercept method (d=1.74L). OM and SEM images show that all the eutectic phases in the cast alloy are treated in magnesium matrix except the dense cuboid-shaped phases, as shown in Fig. 1(b). The semi-quantitative energy-dispersive X-ray spectra (EDX) result shows that the composition of the cuboid-shaped phase is close to the Mg_5Y phase. However, the Mg_5(Gd, Y) phases in a Mg−15Gd−5Y−0.5Zr alloy have been completely dissolved into the magnesium matrix after solution treatment at 525 °C for 12 h [25]. The reason for a large number of cuboid-shaped phases remained in this experiment may be due to the shorter solid solution time. Figure 1(d) shows the macro-texture of the solution-treated alloy. The (0002) pole figure shows that it has a random texture with a maximum intensity of 8.63 multiples at random, which should be ascribed to the several grains with large sizes after solution treatment.

3.2 Microstructure of as-rolled WE43 alloy

Figure 2 shows the influence of the last pass rolling reduction on the microstructure of WE43 alloy after hot rolling. The as-rolled alloy after slight rolling reduction (2%) showed nearly a casting microstructure with no obvious dynamic recrystallization occurred, as shown in Fig. 2(a). In addition, a few convex lenticular twins were observed within individual grains, as indicated by the white arrow in Fig. 2(a), and no recrystallized grains were observed within the twins. These twins with convex lenticular morphology were identified as $\{10\bar{1}2\}$ extension twins from the special boundary map. With increasing rolling reduction, the microstructure of the rolled sheets changed significantly. More narrow twins intersected with each other were produced at larger rolling reductions (12% and 20%).

SEM images of the rolled sheets with different rolling reductions are shown in Fig. 3. A semi-quantitative EDX analysis showed that the composition of the cuboid-shaped phase after rolling was also similar to Mg_5Y, as shown in Fig. 3(d), indicating that the cuboid-shaped phase

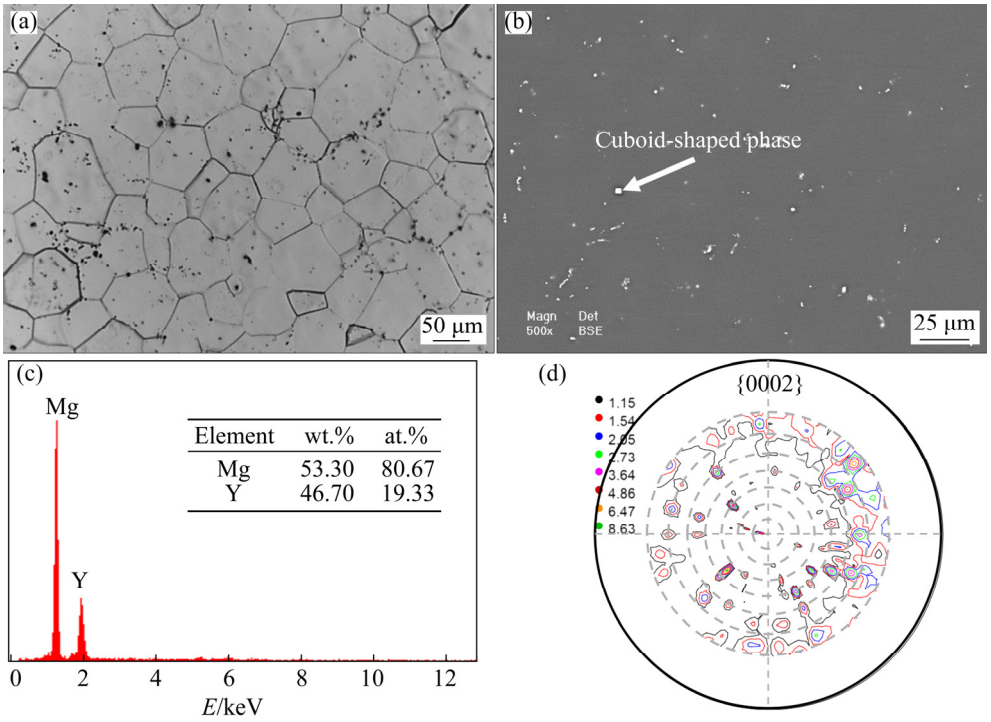

Fig. 1 Microstructure of WE43 alloy after solution treatment: (a) OM image; (b) SEM image; (c) EDX result of cuboid-shaped phase; (d) (0002) pole figure

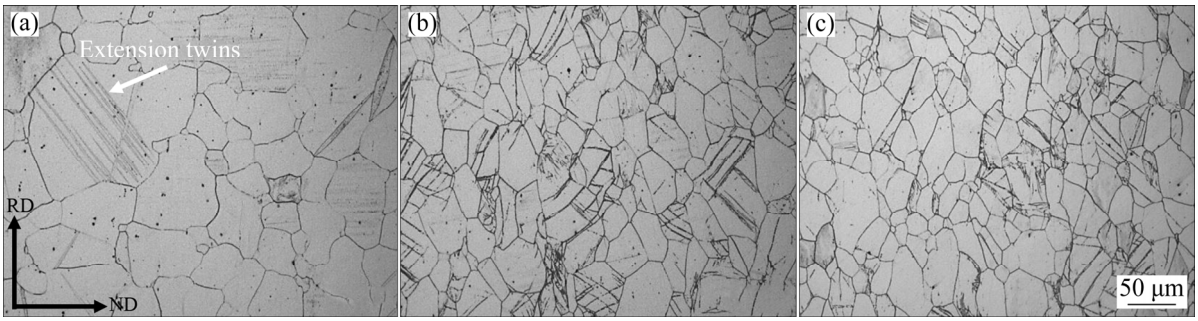

Fig. 2 OM images of as-rolled sheets with different rolling reductions at last pass: (a) S1; (b) S2; (c) S3

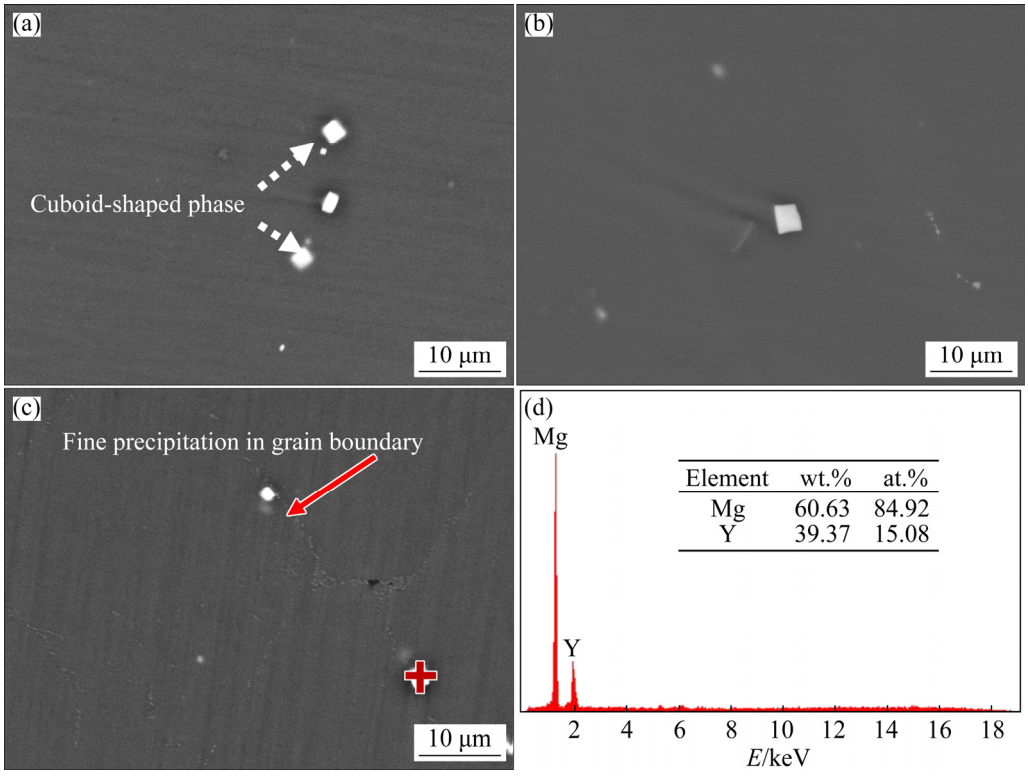

Fig. 3 SEM images of WE43 alloy with different rolling reductions at last pass: (a) S1; (b) S2; (c) S3; (d) EDX result of cuboid-shaped phase in (c) indicated by red cross-shape

was stable during the rolling process. Only cuboid-shaped phases were observed in S1 (2%) and S2 (12%), as shown in Figs. 3(a) and (b). However, a few fine precipitated phases with dimension of ~200 nm at GBs were found in the S3 (20%). CHOUDHURI et al [26] identified the fine precipitated phases at GBs in WE alloy as β phases (f.c.c) which have a habit plane of $\{1\,\bar{1}00\}_{Mg}$, and an orientation relationship with α-Mg matrix of $(\bar{1}11)_{\beta}//(1\,\bar{1}00)_{\alpha}$ and $[110]_{\beta}//[0001]_{\alpha}$.

Figure 4 shows the macro-texture of the rolled sheets with different rolling reductions. The rolling direction (RD) and transverse direction (TD) are all the same as shown in Fig. 4(a). It can be observed that the type of macro-textures changed as the rolling reduction increases, but none of them showed a typical basal texture or RE texture which usually formed in rolled magnesium alloy sheets [16,22]. The formation of such kinds of non-basal texture was associated with the incomplete recrystallization microstructure containing a few twins, and many deformed cast grains after rolling. Most of the microstructure after rolling remains as-cast grains, as shown in Fig. 2, so the macro-texture did not change significantly compared to that of the cast alloy, as shown in Fig. 1(d). Texture

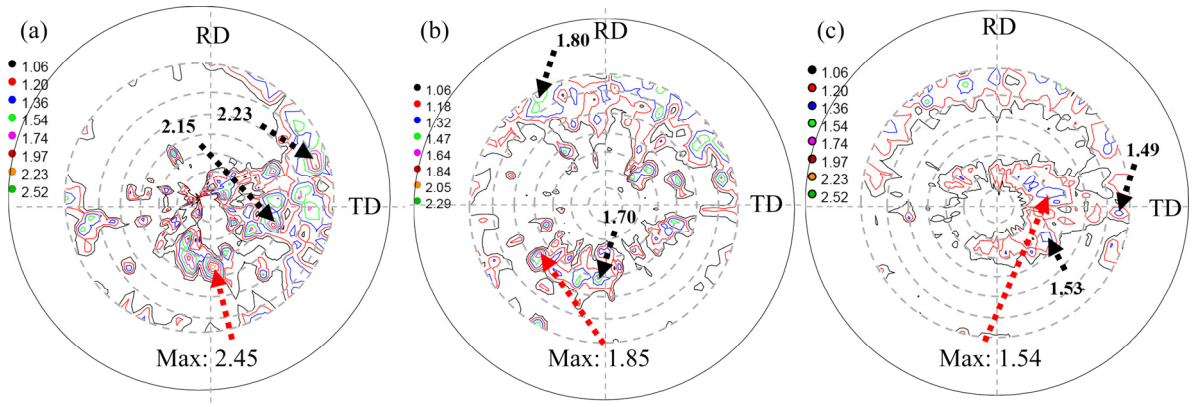

Fig. 4 (0002) macro-texture evolution of WE43 alloy rolled at 480 °C: (a) S1; (b) S2; (c) S3

peaks in the cast alloy were rarely distributed within 40°, after rolling the texture peaks were aligned towards the basal pole, and the distribution of the texture peaks changed with rolling reduction. Variations in macro-texture may be related to the orientation change caused by recrystallization orientated nucleation, twining, and dislocation slip during rolling, i.e., the basal pole of recrystallized grains tended to be parallel to normal direction (ND).

Figures 5(a, d, g) show the grain boundary maps of the alloy rolled at different rolling reductions. Various types of special boundaries ($\{10\bar{1}2\}$ extension twin boundary, $\{10\bar{1}1\}$ compression twin boundary, $\{10\bar{1}1\}-\{10\bar{1}2\}$ double twin boundary) were identified by different colors. The inverse pole figure (IPF) maps are shown in Figs. 5(b, e, h), representing the grain orientation. Figures 5(c, f, i) show the misorientation angle distribution maps of specimens with different rolling reductions. The grain sizes were counted by the linear intercept method (d=1.74L) and dramatically decreased from S1 to S2 (from 67 to 38 μm), while no significant refinement from S2 to S3, as shown in Fig. 6(a).

It can be sure that mainly $\{10\bar{1}2\}$ extension twinning was activated at a rolling reduction of 2% from Fig. 5(a). The corresponding twin boundary volume fraction as shown in Fig. 6(b) indicated that the $\{10\bar{1}1\}$ compression twin boundary and $\{10\bar{1}1\}-\{10\bar{1}2\}$ double twin boundary were minimal, and there were many low angle grain boundaries (LAGBs) within grains. Thus, the contribution of twinning to plastic deformation was not significant due to its relatively small number fraction and the main deformation mechanism was dislocation slip. In addition to the increase of $\{10\bar{1}2\}$ extension twin boundary, $\{10\bar{1}1\}$ compression twin boundary and $\{10\bar{1}1\}-\{10\bar{1}2\}$ double twin boundary appeared and increased with the rolling reduction as shown in Fig. 6(b). Figure 6(c) shows that the number fraction of LAGBs is the largest among all specimens, especially in S2 and S3 which have a large rolling reduction, as can be seen from Figs. 5(c, f, i). The predominance of LAGBs suggests that the deformation produced numerous dislocations and hence dislocation slip dominated the deformation. Figure 6(b) shows that the number fraction of $\{10\bar{1}2\}$ extension twin boundary in S3 drastically falls while that of $\{10\bar{1}1\}-\{10\bar{1}2\}$ double twin boundary rises in comparison to S1 and S2. Meanwhile, the number fraction of LAGBs within grains increases compared with S2.

The hardness of the rolled sheets increases with increasing rolling reduction, as shown in Fig. 6(d). The rolling reduction increased from 2% to 12% with an 11.5% improvement in hardness, but there was a slight increase in hardness from 12% to 20%, which corresponds to the rise of the number fraction of LAGBs. The surged LAGBs from S1 to S2 strengthened the dislocation−dislocation interaction, leading to work hardening, thereby enhanced the strength and hardness of the rolled sheets. However, the number fraction of LAGBs barely increased from S2 to S3, so work hardening was not apparent and there was only a slight improvement in hardness.

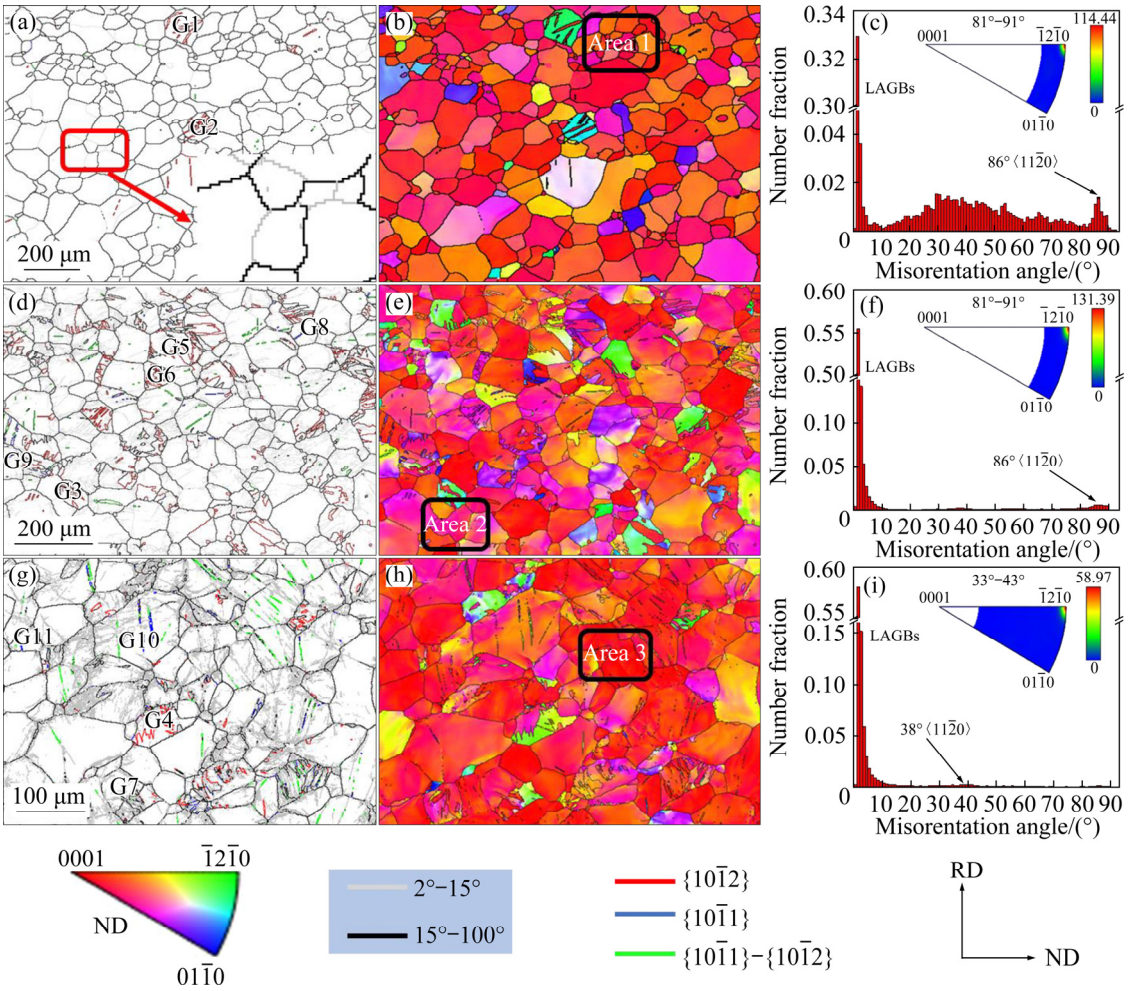

Fig. 5 Grain boundary maps (a, d, g) and corresponding inverse pole figures (b, g, h), and misorientation angle distribution maps of specimens (c, f, i) with different deformations at last pass: (a, b, c) S1; (d, e, f) S2; (g, h, i) S3

4 Discussion

4.1 Slip modes

Kernel average misorientation (KAM) and in-grain misorientation axes (IGMA) are two parameters to describe the misorientation of a crystal [27−29]. KAM shows the deviation of the local orientation to the surrounding orientation. The local misorientation is caused by the pile-up of dislocations, so the KAM value represents the dislocation density. In IGMA figures, the slip system rotating around the ⟨0001⟩ axis is identified as prismatic ⟨*a*⟩ slip. Unfortunately, basal slip and pyramidal slip are indistinguishable by IGMA.

Figure 7 shows the KAM maps of the as-rolled WE43 sheets from Figs. 5(a, d, g). And, their corresponding relative frequency and average KAM value are shown in Figs. 7(d, e). The map sets the max-misorientation angle to 5°. From the KAM maps, it was observed that the dislocation density of S2 and S3 was significantly higher than that of S1, which was attributed to the larger rolling reduction. The higher dislocation density suggests that many LAGBs were formed by the pile-up of dislocation, which was consistent with the statistics results of LAGBs, as shown in Fig. 6(c).

Figure 8 shows the IGMA maps of as-rolled WE43 sheets, and the misorientation axes of all the material-point pairs are in the range of 1.3°−2°. All three specimens had the maximum axis density (over 2 mud) near the ⟨0001⟩ axis, indicating that prismatic ⟨*a*⟩ slip was heavily activated during the rolling process [29]. Whereas, the misorientation axes were also distributed near the ⟨uvt0⟩ axes besides the ⟨0001⟩ axis at small rolling reduction (2%). As the rolling reduction continued to increase (12% and 20%), the distribution of orientation axes

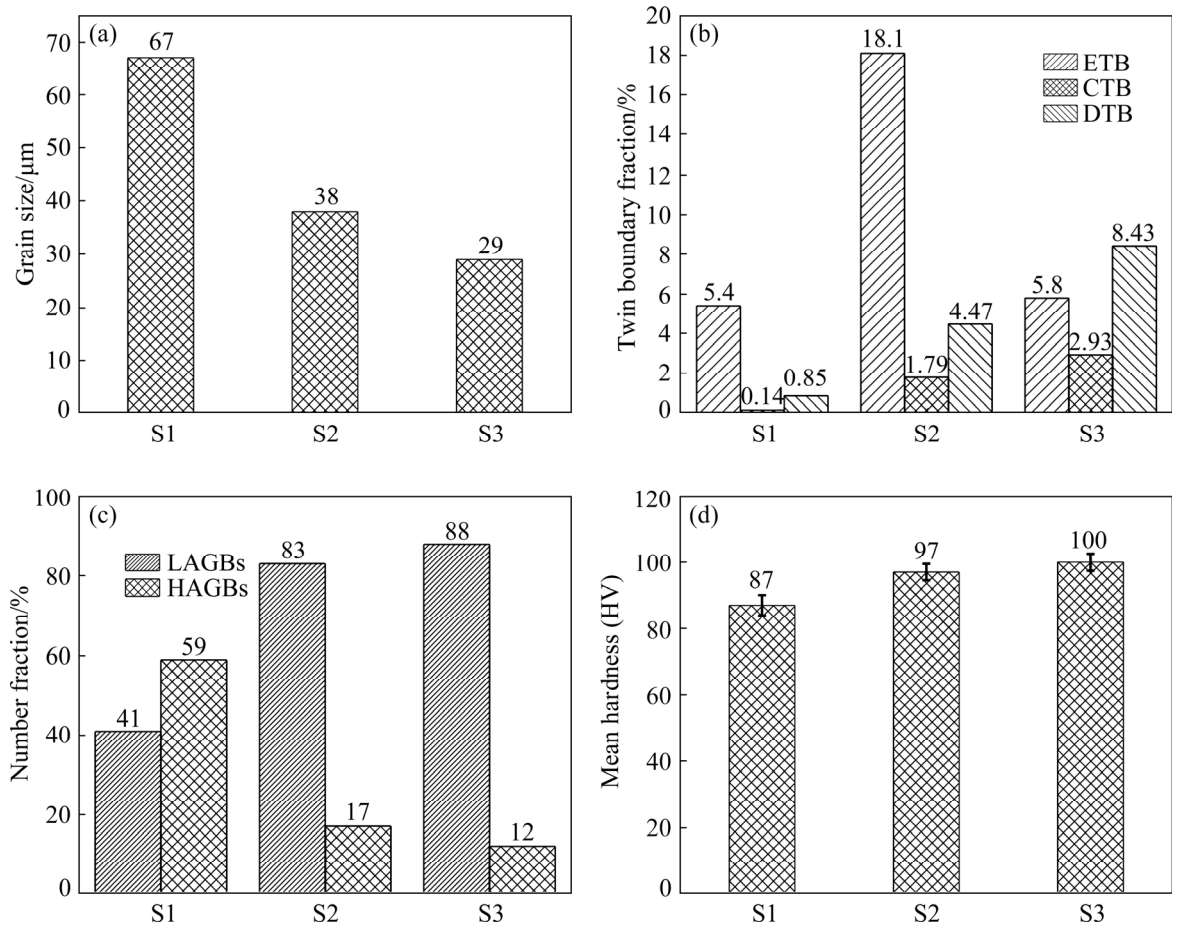

Fig. 6 Statistics of average grain size (a), twin boundary fraction of rolled sheets with different deformations (b), statistics of LAGBs and HAGBs (high angle grain boundaries) fraction (c), and Vickers hardness of rolled sheets (d) (ETB−Extension twin boundary; CTB−Compression twin boundary; DTB−Double twin boundary)

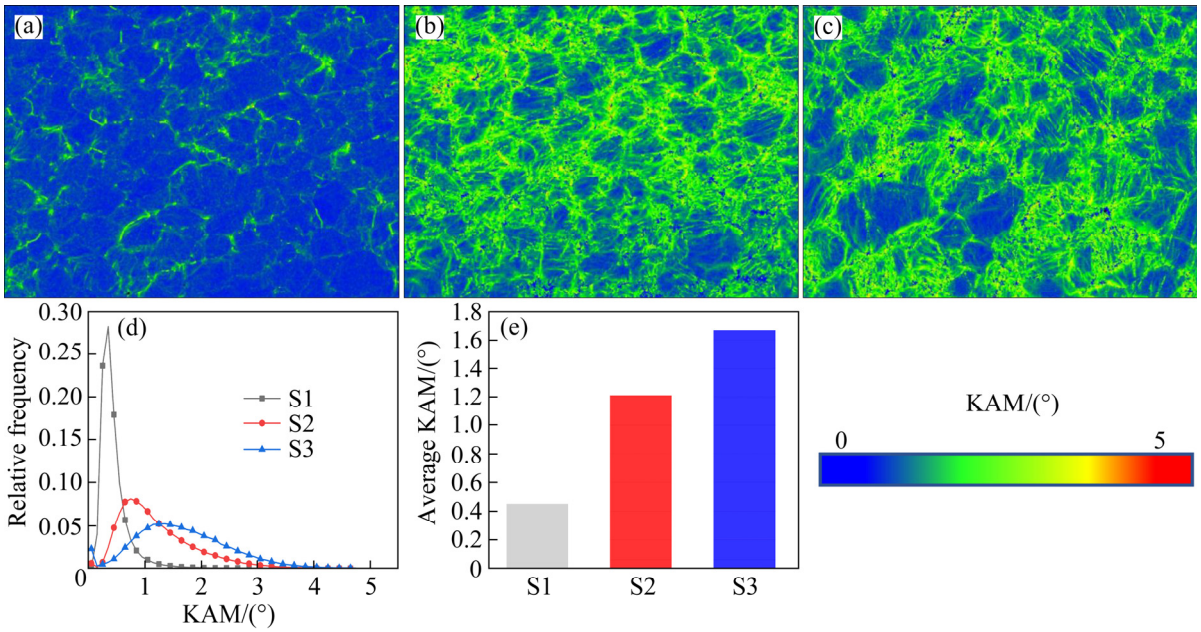

Fig. 7 KAM maps (a, b, c) from Figs. 5(a, d, g), respectively, and corresponding relative frequency (d) and average KAM value (e)

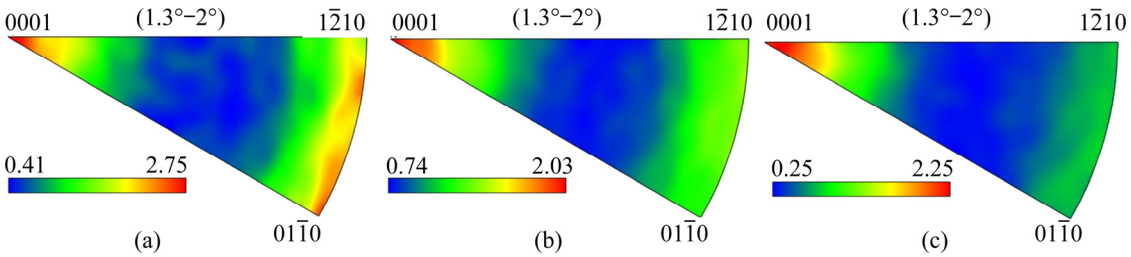

Fig. 8 In-grain misorientation axes (IGMA) maps of S1 (a), S2 (b) and S3 (c)

slowly converged around the ⟨0001⟩ axis, suggesting that prismatic ⟨*a*⟩ was the predominantly activated slip system to accommodate the large rolling deformation when rolling reduction was over 12%, as shown in Figs. 8(b) and (c). The high activity of prismatic ⟨*a*⟩ was probably because the CRSS of prismatic ⟨*a*⟩ slip decreased in the same order of magnitude of basal slip caused by the addition of RE elements as well the high rolling temperature [30]. The hot compression of AZ31 and Mg−Gd magnesium alloys at 400 °C revealed that the misorientation axes of AZ31 were concentrated around ⟨uvt0⟩, while the misorientation axis of Mg−Gd alloy was concentrated around ⟨0001⟩ [31]. This indicates that the addition of RE elements facilitates the activation of prismatic ⟨*a*⟩ slip during the thermal deformation of magnesium alloys. In addition, as the rolling reduction increased, the basal ⟨*a*⟩ slip alone was not sufficient to mediate the strain, so the auxiliary regulation of other slip systems was required.

Figure 9 shows the average Schmid factor (SF) for different slip systems. Although the rolling process was in a state of triaxial stress, the main plastic deformation was along the RD and ND.

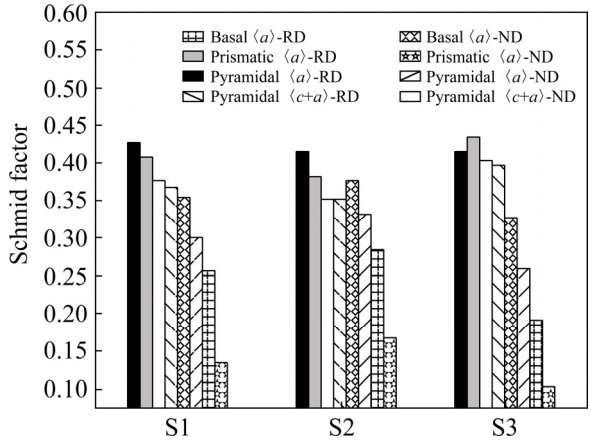

Fig. 9 Average Schmid factor statistics of different slip systems and loading directions parallel to RD and ND

Hereafter, in the present work, the average SF was calculated only when the loading direction was along the RD and ND. The SF of the prismatic ⟨*a*⟩ slip was the highest when the loading direction was RD, and thus was the most likely system to be activated, which corresponds well to the IGMA results. Both the average SF and IGMA analysis indicated that prismatic ⟨*a*⟩ slip was the dominant deformation mechanism during rolling WE43 at 480 °C, especially at large strain.

4.2 Effect of rolling reduction on twinning behavior

Several typical twined grains (G1−G4) were selected from Figs. 5(a, d, g), and the IPF maps are shown in Fig. 10, where M and T represent the matrix grain and twin band, respectively. From the grain boundary map, it was determined that {10$\bar{1}$2} extension twinning occurred in all four grains (G1−G4). The relative orientation of the matrix (indicated by black rectangles) and activated twins (blue circles) in G1−G4 are shown in the {0001} pole figures, as shown in Figs. 10(b, e, h, k). The relative locations of the six theoretical twinning planes of the matrix are illustrated in the {10$\bar{1}$2} pole figures as shown in Figs. 10(c, f, i, l) to determine which twin variants can be activated. The activated twin variants in G1−G4 were observed as para-positions from {10$\bar{1}$2} pole figures (T1 and T2, T3 and T4 in Fig. 10(a), T1 and T2 in Fig. 10(d), T1 and T2 in Fig. 10(g)). In addition, the relative orientation of the matrix to the twin variants is illustrated in Fig. 10. The three-dimensional orientation of the matrix and twin variants is shown on the map. Table 1 lists the main twin type present in specimens according to Fig. 5 [6].

In S1, only a few twins were activated in the grains due to the slight rolling reduction, as shown in Fig. 5(a). G1 and G2 were selected from the grains within Fig. 5(a), where twinning occurred,

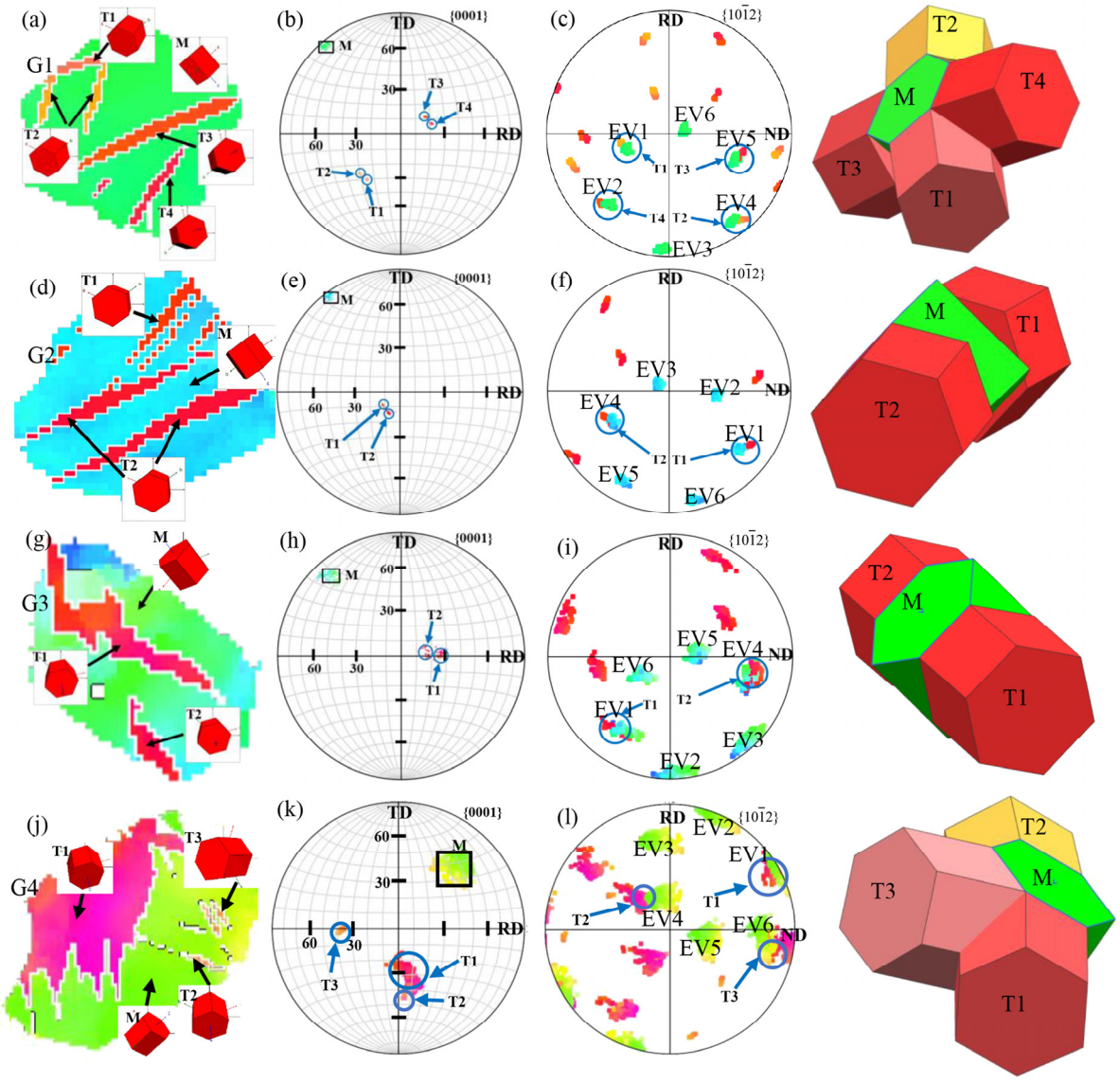

Fig. 10 Pole figures selected from S1 (a, d) and from S2 and S3 (g, j), corresponding {0001} pole figures (b, e, h, k), and corresponding $\{10\bar{1}2\}$ pole figure (c, f, i, l) (The direction of projection was marked on the respective projection map. EV1−EV6 in (c, f, i, l) represent six twin variants)

Table 1 Misorientation between matrix and primary or secondary twin in Fig. 5

Type of twin	Misorientation angle/(°)	Axis
$\{10\bar{1}2\}$	86	$\langle 1\bar{2}10\rangle$
$\{10\bar{1}1\}$	56	$\langle 1\bar{2}10\rangle$
$\{10\bar{1}1\}-\{10\bar{1}2\}$	38	$\langle 1\bar{2}10\rangle$

the corresponding pole figures (Figs. 10(b, e)) show that there are several twin variants activated, e.g., G1 activated four $\{10\bar{1}2\}$ extension twin variants (EV) and G2 activated two variants. A large number of $\{10\bar{1}2\}$ extension twins were activated in S2, which was different from S1, and the thickness of twin bands increased (the thickness of twin bands was defined as the maximum distance between two adjacent 86° peaks in a twin [32]). In addition, most grains contain only one $\{10\bar{1}2\}$ extension twin variant, while only a few grains activated multiple variants. As shown in Figs. 10(g, h), two twin variants were activated in the selected G3 from Fig. 5(c), and the simultaneous activation of $\{10\bar{1}1\}$ compression twinning and $\{10\bar{1}1\}-\{10\bar{1}2\}$ double twinning were also observed in the other grains. In S3, the $\{10\bar{1}1\}-\{10\bar{1}2\}$ double twinning was mainly activated, while the number fraction of the $\{10\bar{1}2\}$ extension twin boundary decreased sharply. The evolution of the twins from

S1 to S3 is as follows: as the rolling reduction increased, the $\{10\bar{1}2\}$ extension twins nucleated and grew and then rapidly consumed the parent matrix due to the high mobility of extension twin boundary, causing the basal plane of the parent matrix to turn in a direction perpendicular to the ND, which makes it easier for the activation of compression twinning (the *c*-axis of the crystal was compressed) and $\{10\bar{1}1\}-\{10\bar{1}2\}$ double twin in large volumes with continually increasing of rolling reduction.

$\{10\bar{1}2\}$ extension twin has six variants, and only the crystallographic plane with the highest SF can be twinned when subjected to an exerted force. Some studies suggest that the selection of $\{10\bar{1}2\}$ extension twin variants follows the Schmid law [23,32,33]. However, different opinions also have been reported [34−36]. Several grains containing extension twins were selected from Figs. 5(a, d, g) named G1−G7 and were used to discuss whether the activation of the $\{10\bar{1}2\}$ extension twin variants follows the Schmid law. The SF values of the six $\{10\bar{1}2\}$ extension twin variants were calculated according to Ref. [23] and the results are shown in Table 2 (the calculated values were expressed as absolute values). It was worth noting that only compression stress along the ND direction was taken into account when calculating the SF [23]. The SF values in Table 2 show that the activated $\{10\bar{1}2\}$ extension twin variants had the largest SF among the six variants, indicating that the selection of the $\{10\bar{1}2\}$ extension twin variants follows the Schmid law, and the same result was also obtained in our previous work [32]. It should be noted that SF of the activated $\{10\bar{1}2\}$ extension twin variants in a few grains was not the maximum value but also ranked in the top three, probably due to the geometric compatibility factor (m'), which is a factor described compatibility or modulating strain [37].

The SF for the $\{10\bar{1}1\}$ compression twin variants was calculated in the same way as the SF for the $\{10\bar{1}2\}$ extension twin variants [23]. Only $\{10\bar{1}1\}$ compression twinning occurred in S2 and S3, they were selected from Figs. 5(d, g) to calculate the SF for $\{10\bar{1}1\}$ compression twin variants and the results are listed in Table 3. It was evident that the SF of the activated $\{10\bar{1}1\}$ compression twin variants was not the largest among the SFs of the six variants, and this non-Schmid behavior indicated that the selection of the $\{10\bar{1}1\}$ compression twin variants did not follow the Schmid law, which was different from that in AZ31 [23].

Table 2 Schmid factor (absolute value) of six theoretical $\{10\bar{1}2\}$ extension twinning variants (EV1−EV6) of several grains selected from Fig. 10

Twin variant	EV1	EV2	EV3	EV4	EV5	EV6
G1	0.312*	0.438*	0.005	0.305*	0.433	0.006
G2	0.470*	0.272	0.030	0.470*	0.270	0.033
G3	0.383*	0.009	0.272	0.347*	0.038	0.264
G4	0.200*	0.101	0.220	0.224*	0.093	0.244*
G5	0.218*	0.124	0.174	0.138	0.051	0.159
G6	0.457*	0.113	0.065	0.452	0.101	0.076
G7	0.268*	0.229	0.071	0.325	0.284	0.061

*: Activated twinning variant

Table 3 Schmid factor (absolute value) of six theoretical compression twinning variants (CV1−CV6) of several grains selected from Fig. 10

Twin variant	CV1	CV2	CV3	CV4	CV5	CV6
G8	0.292*	0.264	0.321	0.139	0.242	0.150
G9	0.242*	0.244	0.265	0.163	0.207	0.261
G10	0.331*	0.000	0.000	0.183	0.424	0.445
G11	0.233*	0.104	0.276	0.472	0.485	0.449

*: Activated twinning variant

4.3 Recrystallization of WE43 alloy rolled at 480 °C

Figure 11 shows the EBSD IPF subset maps from the grain orientation spread (GOS) showing the recrystallization grains. It is interesting to note that hardly any DRX grains were found in the rolling reduction of 12% and 20%. However, a considerable number of LAGBs cross-entangled within the grains of S2 and S3 fragmented the grains into several sub-grains, and the in-grain misorientation gradually increased, as shown in Figs. 12(b, c). This recrystallization process was the same as that of CDRX reported by SITDIKOV and KAIBYSHEV [38]. The new recrystallized grains were formed from the three-dimensional array of deformed stable LAGBs, which gradually transformed into HAGBs [39]. Unfortunately, the current experimental results did not show the typical

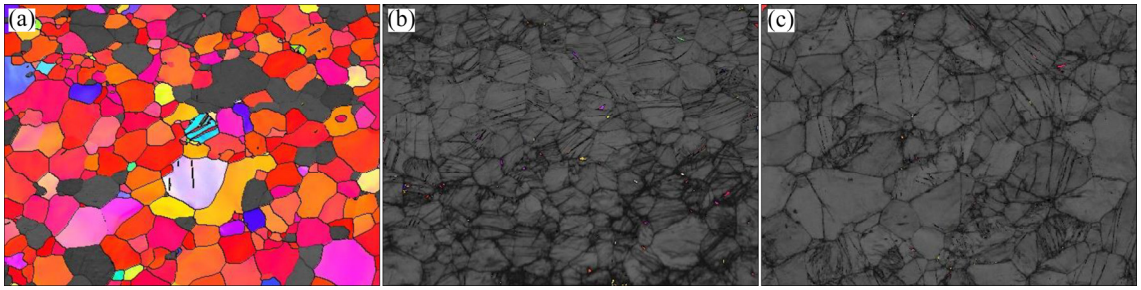

Fig. 11 EBSD IPF subset maps form grain orientation spread (GOS) showing recrystallization at different rolling reductions: (a) 2%; (b) 12%; (c) 20%

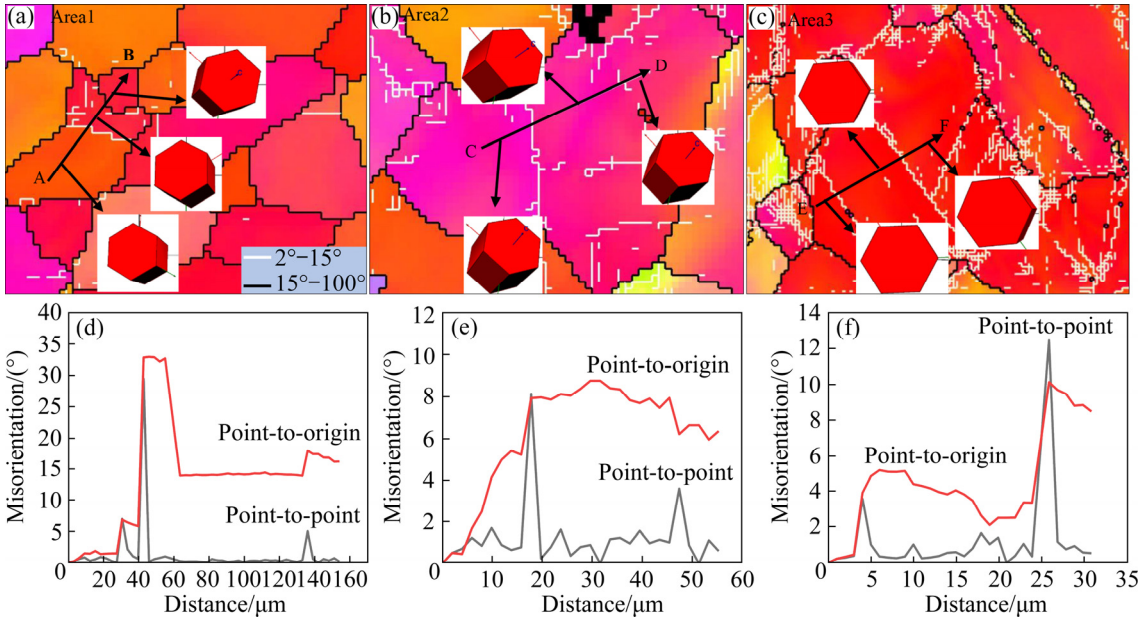

Fig. 12 EBSD results: (a, b, c) Selected from Figs. 5(b, e, h); (d, e, f) Line profiles of misorientation angle along black arrows AB, CD and EF in (a, b, c), respectively

necklace-like CDRX grains due to the smaller rolling reduction, which did not supply sufficient storage energy for DRX behavior, and the same phenomenon was also observed by FATEMI and PAUL [40]. From the results of this work, it is assumed that an increased single roll reduction is required to achieve grain refinement.

Due to the slight rolling reduction (2%), S1 can be approximated as the annealed state and its internal recrystallization can be recognized as the recrystallization that occurred during the annealing process. From the EBSD results, the misorientation angle of the LAGBs within the matrix transformed to form HAGBs and static recrystallization (SRX) occurred, as shown in Fig. 12(a). This SRX process was similar to that of DDRX, which involves the development of HAGBs through nucleation and the growth of new grains to eventually consume the deformed matrix.

5 Conclusions

(1) After the last pass rolling, the microstructure mainly consists of twins and low-angle grain boundaries. Only $\{10\bar{1}2\}$ extension twinning was activated at a rolling reduction of 2%, while many $\{10\bar{1}1\}-\{10\bar{1}2\}$ double twinning and $\{10\bar{1}1\}$ compression twinning were activated when the rolling reduction was over 12%. Moreover, the behavior of the $\{10\bar{1}2\}$ extension twin variants followed the Schmid law while $\{10\bar{1}1\}$ compression twin variants not.

(2) Twinning and dislocation slip took place during the rolling process, but the deformation mechanism varied according to the rolling reduction. At a rolling reduction of 2%, the deformation was mainly dependent on dislocations slip, while at rolling reductions of 12% and 20%, the deformation

was mediated by a combination of dislocations slip and twins. In addition, prismatic ⟨*a*⟩ slip became more active to accommodate the strain, especially at a large rolling reduction.

(3) Almost no DRX grains were found even at a reduction of 20%. The reason for the delayed recrystallization was related to the fact that the rolling reduction required for recrystallization has not been reached. Increasing single pass rolling reduction was required for DRX to occur.

Acknowledgments

This work was financially supported by the Natural Science Foundation of Liaoning Province, China (No. 2020-MS-004), the National Natural Science Foundation of China (Nos. 51601193, 51701218), the National Key Research and Development Program of China (No. 2016YFB0301104), and the State Key Program of National Natural Science of China (No. 51531002).

References

[1] LUO A A. Magnesium casting technology for structural applications [J]. Journal of Magnesium and Alloys, 2013, 1: 2−22.

[2] MORDIKE B L, EBERT T. Magnesium: properties−applications−potential [J]. Materials Science and Engineering: A, 2001, 302: 37−45.

[3] WANG Yuan-bo, ZHAO Wei, LI Liang, AN Jian. Relation of normal load with test temperature at mild–severe wear transition state for Mg−Gd−Y−Zr alloy [J]. Transactions of Nonferrous Metals Society of China, 2021, 31: 2986−2998.

[4] LU Zheng-Guan, WU Jie, XU Lei, YANG Rui. Powder size influence on tensile properties and porosity for PM Ti_2AlNb alloy prepared by hot isostatic pressing [J]. Acta Metallurgica Sinica (English Letters), 2019, 32: 1329−1336.

[5] SUSAN D F, CRENSHAW T B, GEARHART J S. The effects of casting porosity on the tensile behavior of investment cast 17-4PH stainless steel [J]. Journal of Materials Engineering and Performance, 2015, 24: 2917−2924.

[6] GUAN D K, RAINGORTH W M, GAO J H, SHARP J, WYNNE B, MA L E. Individual effect of recrystallisation nucleation sites on texture weakening in a magnesium alloy: Part 1—Double twins [J]. Acta Materialia, 2017, 135: 14−24.

[7] GAO Lei, CHEN Rong-shi, HAN En-hou. Fracture behavior of high strength Mg−Gd−Y−Zr magnesium alloy [J]. Transactions of Nonferrous Metals Society of China, 2010, 20: 1217−1221.

[8] GU Kan, ZENG Xiao-qin, CHEN Bin, WANG Ying-xin. Effect of double aging on mechanical properties and microstructure of EV31A alloy [J]. Transactions of Nonferrous Metals Society of China, 2021, 31: 2606−2614.

[9] KANG Y H, YAN H, CHEN R S. Creep behavior and microstructure evolution of sand-cast Mg−4Y−2.3Nd−1Gd−0.6Zr alloy crept at 523−573 K [J]. Journal of Materials Science & Technology, 2017, 33: 79−89.

[10] SALANDARI-RABORI A, ZAREI-HANZAKI A, FATEMI S M, GHAMBARI M, MOGHADDAM M. Microstructure and superior mechanical properties of a multi-axially forged WE magnesium alloy [J]. Journal of Alloys and Compounds, 2017, 693: 406−413.

[11] WAN Ying-chun, XU Shi-yuan, LIU Chu-ming, GAO Yong-hao, JIANG Shu-nong, CHEN Zhi-yong. Enhanced strength and corrosion resistance of Mg−Gd−Y−Zr alloy with ultrafine grains [J]. Materials Letters, 2018, 213: 274−277.

[12] XU Bing-qian, SUN Jia-peng, YANG Zhen-quan, HAN Jing, FU Yan-tao, JIANG Jing-hua, MA Ai-bin. A near-isotropic ultrafine-grained Mg−Gd−Ag alloy with high strength−ductility synergy [J]. Journal of Materials Research and Technology, 2020, 9: 13616−13624.

[13] WANG J G, HSIUNG L M, NIEH T G, MABUCHI M. Creep of a heat treated Mg−4Y−3RE alloy [J]. Materials Science and Engineering A, 2001, 315: 81−88.

[14] LIANG Shu-quan, GUAN Di-kai, CHEN Liang, GAO Zhao-he, TANG Hui-xiang, TONG Xu-ting, XIAO Rui. Precipitation and its effect on age-hardening behavior of as-cast Mg−Gd−Y alloy [J]. Materials & Design, 2011, 32: 361−364.

[15] GUAN D K, RAINFORTH W M, MA LE, WYNNE B, GAO J H. Twin recrystallization mechanisms and exceptional contribution to texture evolution during annealing in a magnesium alloy [J]. Acta Materialia, 2017, 126: 132−144.

[16] HUANG X S, SUZUKI K, CHINO Y. Different annealing behaviours of warm rolled Mg−3Al−1Zn alloy sheets with dynamic recrystallized microstructure and deformation microstructure [J]. Materials Science and Engineering A, 2013, 560: 232−240.

[17] KIM D W, SUH B C, SHIM M S, BAE J H, KIM D H, KIM N J. Texture evolution in Mg−Zn−Ca alloy sheets [J]. Metallurgical and Materials Transactions A, 2013, 44(7): 2950−2961.

[18] Al-SAMMAN T. Modification of texture and microstructure of magnesium alloy extrusions by particle-stimulated recrystallization [J]. Materials Science and Engineering A, 2013, 560: 561−566.

[19] ZHANG Zhi, ZHANG Jing-huai, XIE Jin-shu, LIU Shu-juan, HE Yu-ying, WANG Ru, FANG Da-qing, FU Wei, JIAO Yun-lei, WU Rui-zhi. Significantly enhanced grain boundary Zn and Ca co-segregation of dilute Mg alloy via trace Sm addition [J]. Materials Science and Engineering A, 2022, 831: 142259.

[20] MACKENZIE L W F, DAVIS B, HUMPHREYS F J, LORIMER G W. The deformation, recrystallisation and texture of three magnesium alloy extrusions [J]. Materials Science and Technology, 2007, 23: 1173−1180.

[21] ASGARI H, ODESHI A G, SZPUNAR J A. On dynamic deformation behavior of WE43 magnesium alloy sheet under shock loading conditions [J]. Materials & Design, 2014, 63: 552−564.

[22] BARNETT M R, NAVE M D, BETTLES C J. Deformation microstructures and textures of some cold rolled Mg alloys

[J]. Materials Science and Engineering A, 2004, 386: 205−211.
[23] ZHANG Zhen, WANG Ming-pu, JIANG Nian, LI Shu-mei. Orientation analyses for twinning behavior in small-strain hot-rolling process of twin-roll cast AZ31B sheet [J]. Materials Science and Engineering A, 2010, 527: 6467−6473.
[24] DEL VALLE J A, PÉREZ-PRADO M T, RUANO O A. Accumulative roll bonding of a Mg-based AZ61 alloy [J]. Materials Science and Engineering A, 2005, 410−411: 353−357.
[25] GAO Y, WANG Q D, GU J H, ZHAO Y, TONG Y. Behavior of Mg−15Gd−5Y−0.5Zr alloy during solution heat treatment from 500 to 540 °C [J]. Materials Science and Engineering A, 2007, 459: 117−123.
[26] CHOUDHURI D, MEHER S, NAG S, DENDGE N, HWANG J Y, BANERJEE R. Evolution of a honeycomb network of precipitates in a hot-rolled commercial Mg−Y−Nd−Zr alloy [J]. Philosophical Magazine Letters, 2013, 93: 395−404.
[27] RUI Shao-shi, NIU Li-sha, SHI Hui-ji, WEI Shao-lou, TASAN C C. Diffraction-based misorientation mapping: A continuum mechanics description [J]. Journal of the Mechanics and Physics of Solids, 2019, 133: 103709.
[28] WRIGHT S I, NOWELL M M, FIELD D P. A review of strain analysis using electron backscatter diffraction [J]. Microscopy and Microanalysis, 2011, 17: 316−329.
[29] CHUN Y B, BATTAINI M, DAVIES C H J, HWANG S K. Distribution characteristics of in-grain misorientation axes in cold-rolled commercially pure titanium and their correlation with active slip modes [J]. Metallurgical and Materials Transactions A, 2010, 41(13): 3473−3487.
[30] CHAPUIS A, DRIVER JULIAN H. Temperature dependency of slip and twinning in plane strain compressed magnesium single crystals [J]. Acta Materialia, 2011, 59: 1986−1994.
[31] STANFORD N, CALLAGHAN M D, de JONG B. The effect of rare earth elements on the behaviour of magnesium-based alloys: part 1 — Hot deformation behaviour [J]. Materials Science and Engineering A, 2013, 565: 459−468.
[32] LU S H, WU D, CHEN R S, HAN E H. The influence of temperature on twinning behavior of a Mg−Gd−Y alloy during hot compression [J]. Materials Science and Engineering A, 2018, 735: 173−181.
[33] BAO L, SCHUMAN C, LECOMTE J S, PHILIPPE M J, ZHAO X, ESLING C. A study of twin variant selection and twin growth in titanium [J]. Advanced Engineering Materials, 2011, 13: 928−932.
[34] BEYERLEIN I J, CAPOLUNGO L, MARSHALL P E, MCCABE R J, TOMÉ C N. Statistical analyses of deformation twinning in magnesium [J]. Philosophical Magazine, 2010, 90: 2161−2190.
[35] SHI Z Z, ZHANG Y D, WAGHER F, JUAN P A, BERBENNI S, CAPOLUNGO L, LECOMTE J S, RICHETON T. On the selection of extension twin variants with low Schmid factors in a deformed Mg alloy [J]. Acta Materialia, 2015, 83: 17−28.
[36] BARNETT M R, KESHAVARZ Z, BEER A G, MA X. Non-Schmid behaviour during secondary twinning in a polycrystalline magnesium alloy [J]. Acta Materialia, 2008, 56: 5−15.
[37] GUAN D K, WYNNE B, GAO J H, HUANG Y H, RAINFORTH W M. Basal slip mediated tension twin variant selection in magnesium WE43 alloy [J]. Acta Materialia, 2019, 170: 1−14.
[38] SITDIKOV O, KAIBYSHEV R. Dislocation glide and dynamic recrystallization in LiF single crystals [J]. Materials Science and Engineering A, 2002, 328: 147−155.
[39] BEER A G, BARNETT M R. Microstructural development during hot working of Mg−3Al−1Zn [J]. Metallurgical and Materials Transactions A, 2007, 38: 1856−1867.
[40] FATEMI S M, PAUL H. Characterization of continuous dynamic recrystallization in WE43 magnesium alloy [J]. Materials Chemistry and Physics, 2021, 257: 123726.

压下量对 WE43 镁合金变形机理和孪生行为的影响

李乾坤[1,2]，闫 宏[1,2]，陈荣石[1,2]

1. 中国科学院 金属研究所 师昌绪先进材料创新中心，沈阳 110016；
2. 中国科学技术大学 材料科学与工程学院，沈阳 110016

摘 要：研究最后一道次压下量对铸态 WE43 镁合金在 480 ℃直接热轧过程中位错滑移和孪生行为的影响。结果表明，在 480 ℃轧制时柱面⟨*a*⟩滑移始终是主要的滑移模式。另外，不同压下量下激活的孪生类型不同。较小的压下量(2%)下激活的主要是 $\{10\bar{1}2\}$ 拉伸孪生，而在较大的压下量 (12% 和 20%)下激活的主要是 $\{10\bar{1}1\}$ 压缩孪生和 $\{10\bar{1}1\}-\{10\bar{1}2\}$ 二次孪生。Schmid 因子计算表明，$\{10\bar{1}2\}$ 孪晶变体选择遵循 Schmid 定律，而 $\{10\bar{1}1\}$ 孪晶变体选择不遵循 Schmid 定律。即使单道次压下量达到 20%也几乎没有发现动态再结晶晶粒，这可能是因为没有达到动态再结晶所需要的变形量。

关键词：镁合金；变形；孪晶变体；再结晶

(Edited by Xiang-qun LI)